catalysts

MDPI

Article

In-Situ Synthesis of Nb_2O_5/g-C_3N_4 Heterostructures as Highly Efficient Photocatalysts for Molecular H_2 Evolution under Solar Illumination

Faryal Idrees [1,2,3,*], Ralf Dillert [1,2], Detlef Bahnemann [1,2,*], Faheem K. Butt [4] and Muhammad Tahir [3]

1 Institut für Technische Chemie, Gottfried Wilhelm Leibniz Universität Hannover, Callinstrasse 3, D-30167 Hannover, Germany; dillert@iftc.uni-hannover.de
2 Laboratorium für Nano- und Quantenengineering, Gottfried Wilhelm Leibniz Universität Hannover, Schneiderberg 39, D-30167 Hannover, Germany
3 Department of Physics, The University of Lahore, 1-Km Raiwind, Lahore 53700, Pakistan; tahir94@gmail.com
4 Department of Physics, Division of Science and Technology, University of Education, College Road, Township, Lahore 54770, Pakistan; faheem.khurshid@phys.uol.edu.pk
* Correspondence: idrees@iftc.uni-hannover.de (F.I.); bahnemann@iftc.uni-hannover.de (D.B.)

Received: 7 January 2019; Accepted: 7 February 2019; Published: 11 February 2019

Abstract: This work focuses on the synthesis of heterostructures with compatible band positions and a favourable surface area for the efficient photocatalytic production of molecular hydrogen (H_2). In particular, 3-dimensional Nb_2O_5/g-C_3N_4 heterostructures with suitable band positions and high surface area have been synthesized employing a hydrothermal method. The combination of a Nb_2O_5 with a low charge carrier recombination rate and a g-C_3N_4 exhibiting high visible light absorption resulted in remarkable photocatalytic activity under simulated solar irradiation in the presence of various hole scavengers (triethanolamine (TEOA) and methanol). The following aspects of the novel material have been studied systematically: the influence of different molar ratios of Nb_2O_5 to g-C_3N_4 on the heterostructure properties, the role of the employed hole scavengers, and the impact of the co-catalyst and the charge carrier densities affecting the band alignment. The separation/transfer efficiency of the photogenerated electron-hole pairs is found to increase significantly as compared to that of pure Nb_2O_5 and g-C_3N_4, respectively, with the highest molecular H_2 production of 110 mmol/g·h being obtained for 10 wt % of g-C_3N_4 over Nb_2O_5 as compared with that of g-C_3N_4 (33.46 mmol/g·h) and Nb_2O_5 (41.20 mmol/g·h). This enhanced photocatalytic activity is attributed to a sufficient interfacial interaction thus favouring the fast photogeneration of electron-hole pairs at the Nb_2O_5/g-C_3N_4 interface through a direct Z-scheme.

Keywords: Niobium(V) oxide; graphitic carbon nitride; hydrothermal synthesis; H_2 evolution; photocatalysis; heterostructures; Z-Scheme

1. Introduction

Renewable energy sources are currently needed by our society to address the foreseable future energy crisis and growing environmental issues. The production of molecular H_2 through photoelectrochemical or photocatalytic water splitting is a viable replacement of fossil fuels [1]. In the past, due to certain limitations of the most frequently employed photocatalyst, TiO_2, many other photocatalysts have been developed and explored for photocatalytic molecular H_2 evolution. Their significant limitations are the high recombination rate of photogenerated electron-hole pairs and unfavorable band edges, hence their low photocatalytic activity. For favorable band edges, CuO and

Cu_2O are thought of as good alternatives but their stability and effective light absorption present additional issues. Somehow, these issues have been solved by adopting the atomic layer deposition (ALD) technique and doping, etc. [2–4]. The non-toxicity, facile synthesis, high visible light absorption and good physicochemical stability of g-C_3N_4 have made it an amiable photocatalyst [5–9]. However, the fast recombination rate of photogenerated charge carriers has reduced its charismatic effect. Some researchers proposed to solve this problem by forming heterojunctions with TiO_2 [10], WS_2 [11], BiOCl [12] and WO_3 [13,14]. Still, there is considerable scope to develop other photocatalysts, with the particular focus being on facile synthesis, low toxicity, easy accessibility, and, most importantly, high photocatalytic activity [15].

Niobium pentoxide (Nb_2O_5) is an n-type and wide bandgap (3.4 eV) semiconductor, which has been extensively investigated in recent years for electrochemical, photocatalytic, and energy storage applications [16,17]. Its light absorption can be effectively shifted into the visible region by synthesizing composites with small bandgap materials. Noticeably, heterojunctions prepared with small amounts of Nb_2O_5 have shown a significant improvement in the photocatalytic activity of TiO_2 [8], ZnO [18], and g-C_3N_4 [7,9,19]. To date, there are only a few reports regarding the synthesis of g-C_3N_4/Nb_2O_5 heterojunctions and their photocatalytic properties. Y. Z. Hong et al. [19] and Q. Z. Huang et al. [20] have prepared g-C_3N_4/Nb_2O_5 heterojunctions facing, however, considerable limitations concerning the control of the size and shape of Nb_2O_5, and resulting in a rather small specific surface area. Moreover, to the best of our knowledge, Nb_2O_5/g-C_3N_4 heterostructures have so far not been explored for molecular H_2 evolution.

To increase photocatalytic activities, semiconductor-semiconductor heterostructures exhibiting lower recombination rates of photogenerated electron-hole pairs have been studied. Depending on the energetic situation, these heterostructures have been classified as type-II heterostructures and Z-scheme heterostructures, respectively (Figure 1; for a detailed discussion see the Supporting Information) [20–22]. The direct Z-scheme system seems promising for overcoming the limitations associated with enhanced photocatalytic activity, due to the strong oxidation and reduction potential developed at different active sites [21].

As depicted in Figure 1, a conventional type-II heterostructure can easily be converted into a Z-scheme structure by controlling the Fermi level or the band potentials. Moreover, the Fermi level and band potentials can also be modulated to attain the Z-scheme by the addition of suitable hole scavengers such as triethanolamine (TEOA), which has been reported to exhibit a larger H_2 evolution rate than methanol [19,22].

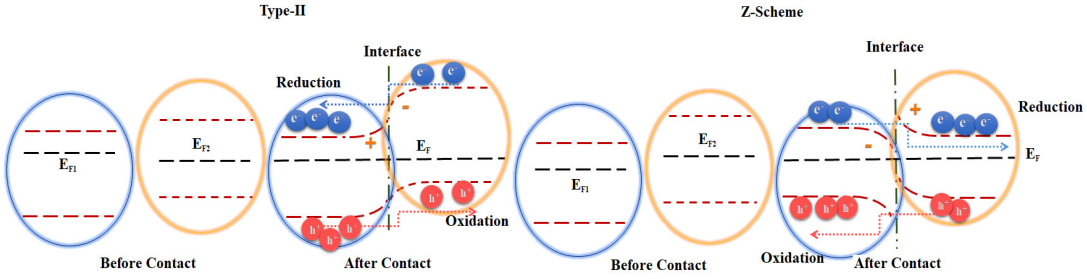

Figure 1. Schematic illustration of Type-II and Z-Scheme systems and their interfacial band bending under bandgap irradiation.

In the present work, Nb_2O_5/g-C_3N_4 Z-scheme heterojunctions were prepared considering their suitable band edges for photocatalytic H_2 production, i.e., Nb_2O_5 (E_{CB} = −0.69 V, E_{VB} = 2.32 V) and g-C_3N_4 (E_{CB} = −1.68 V, E_{VB} = 0.88 V) vs. NHE (pH = 7). In comparison to previous reports, we obtained a controlled shape of the heterojunction with a specific surface area as high as 227 m^2 g^{-1}. The prepared heterojunctions were tested for H_2 evolution without and with deposited platinum (Pt) acting as a cocatalyst, thus faciliating the interfacial electron transfer. The role of hole scavengers in the overall mechanism of the hydrogen evolution reaction was also investigated. A significant increase

in the H_2 evolution rate was observed in the presence of TEOA compared with methanol. These findings have suggested a possible change in the photocatalytic mechanism to increase the evolution rate to such an extent. An excellent H_2 production rate of 110 mmol/h·g was found by employing platinized Nb_2O_5/g-C_3N_4 as the photocatalyst and TEOA as the hole scavenger. Noticeably, the high molecular H_2 rate could also be associated with the tuning of shape, size and structures. The compact interfacial development between Nb_2O_5/g-C_3N_4 also suggested that a Z-scheme system was formed, thus facilitating fast charge carrier separation and excellent photocatalytic performance as compared with simple physical mixing. The effect of different ratios of g-C_3N_4 to Nb_2O_5 has also been studied in detail.

2. Results and Discussion

2.1. Synthesis Procedure

Nb_2O_5 (NBO) and Nb_2O_5/g-C_3N_4 (NBCN) heterostructures were synthesized via a hydrothermal synthesis considering its possible principal advantages such as: (a) attaining porous structures with high surface areas; (b) reagents mixing at the atomic level, and (c) high reaction rates at a low reaction temperature due to the atomic mixing level [23–25]. Thus, a suitable strategy to tune the shape, size, and structure of Nb_2O_5 (NBO) and Nb_2O_5/g-C_3N_4 (NBCN) heterostructures with a high specific surface area and a sufficient contact interface was employed here.

NBO was synthesized via the oxidant-peroxo method (OPM). A niobium salt ($NbCl_5$) was dissolved in diluted nitric acid (HNO_3) to avoid salt residuals. In a second step H_2O_2 was added to the prepared solution to remove chloride ions by an oxidation–reduction process. The resulting yellow solution (pH = 0.5) indicated the presence of the water-soluble niobium peroxo-complex $[Nb(O_2)_4]^{3-}$ (named as NPC). A possible reaction is provided in Figure 2. The decomposition of H_2O_2 into molecular oxygen possibly accelerated the condensation reaction. Amorphous hierarchical spheres of Nb_2O_5 and $Nb_2O_5{\cdot}nH_2O$ were obtained due to an excess amount of H_2O_2. Finally, annealing in the 200–500 °C range resulted in the formation of Nb_2O_5 with adequate composition and controlled morphology.

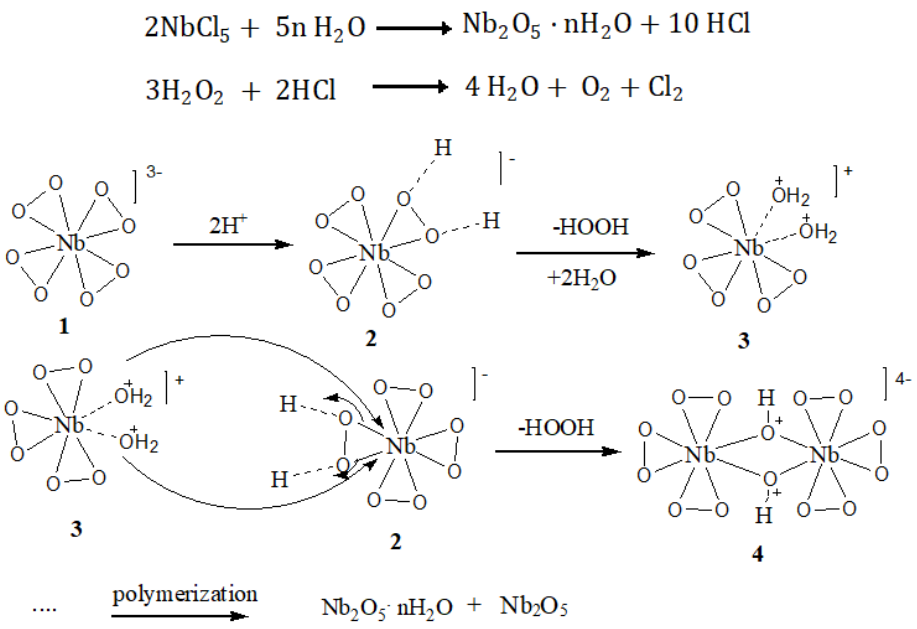

Figure 2. The proposed reaction mechanism for Nb_2O_5 formation.

For the preparation of the heterostructures, a g-C_3N_4 (GCN) suspension was prepared in de-ionised water by 1 h of continuous stirring. The prepared suspension was added to the solution of NPC (as described above) which changed the pH from 0.5 to 0.7. The pH change resulted in a

positive surface charge on GCN. The developed electrostatic attraction between NPC and GCN favors the effective in-situ formation of heterojunctions with a controlled morphology [26]. This procedure was employed to prepare other heterostructures with a different wt % of GCN (as described in the experimental sections). Heterostructures have also been prepared by physical mixing of NBO and g-C_3N_4 (the method is described in the supporting information). A schematic presentation of the synthetic procedure is given in Figure 3.

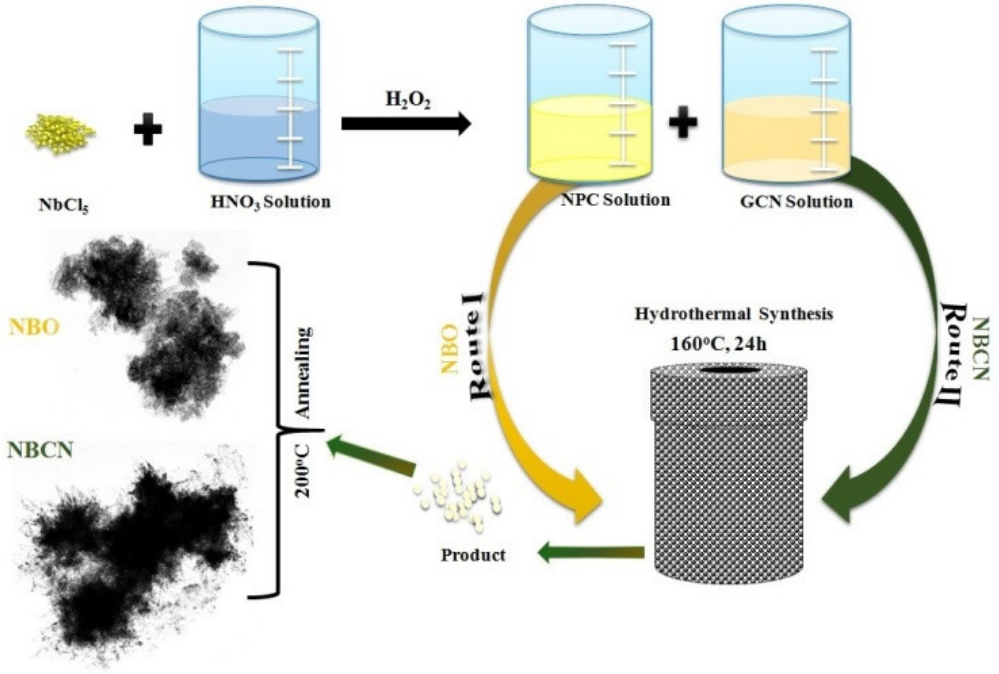

Figure 3. Schematic illustration of the hydrothermal routes followed for Nb_2O_5 (NBO) and Nb_2O_5/g-C_3N_4 (NBCN) synthesis.

2.2. Structural and Morphological Characterization

The phases and the crystal structures of as-prepared NBO, GCN, and NBCN-X were analyzed by XRD (Figure 4). The XRD data obtained for a NBO sample before annealing corresponded to a mixture of niobic acid and amorphous NBO. By annealing at 200 °C the mixture converted to the amorphous pseudohexagonal phase of Nb_2O_5 (TT-NBO, JCPDS#30-0873). No significant change in the phase was observed for samples annealed at temperatures between 200 °C and 400 °C. However, annealing at 500 °C results in the transformation of the amorphous pseudohexagonal phase of NBO in to the pseudohexagonal phase (JCPDS#30-0873) of NBO. The corresponding XRD results are provided in the supporting information in Figure S1. In the XRD of GCN, two peaks are observed at 13.4° and 27.0°, which were associated with the (100) and (002) diffraction planes, respectively. The (100) distinct peak was due to the characteristic inter-planar staking of aromatic systems, while the (002) peak corresponded to the inter-layer structural packing [26]. The XRDs of NBCN-X (X = 1–4) exhibited combinatory characteristic peaks of GCN and NBO. The characteristic peak of GCN (002) become stronger with an increasing amount of GCN, indicating a significant coupling between the GCN and NBO.

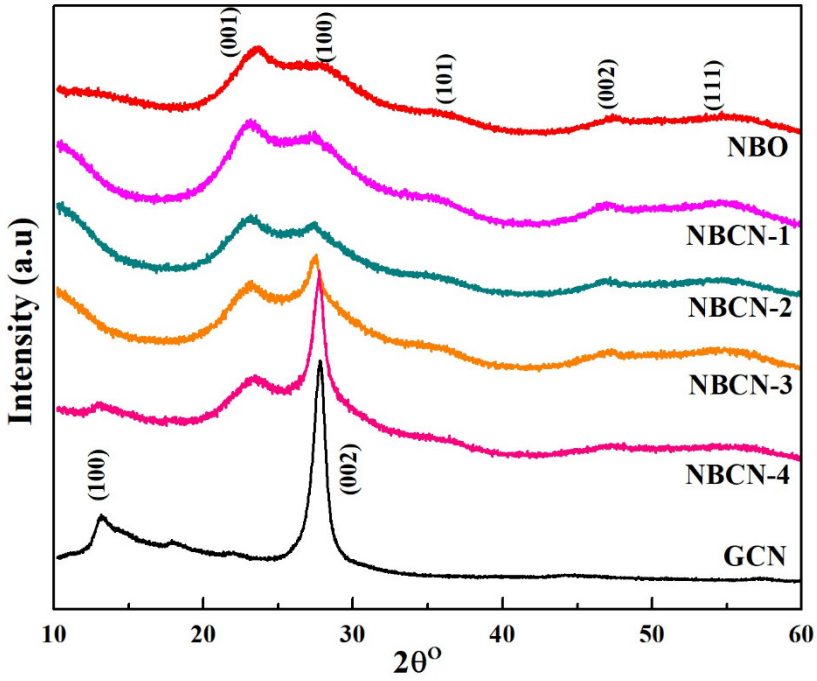

Figure 4. XRD patterns of NBO, g-C_3N_4 (GCN), NBCN-1, NBCN-2, NBCN-3, and NBCN-4.

The FTIR patterns further confirmed the development of compact heterostructure interfaces, as shown in Figure 5a. The amorphous pseudohexagonal phase of NBO possessed slightly distorted NbO_6, NbO_7, and NbO_8 groups and some highly distorted NbO_6 sites (a scheme is provided in Figure 5b). The peak at 665 cm^{-1} has been assigned to the symmetric stretching mode of Nb–O polyhedra (NbO_6, NbO_7, and NbO_8) [27]. The broad shoulder between 850 and 970 cm^{-1} has been assigned to the stretching of Nb=O groups. The removal of coordinated water further distorted the highly distorted NbO_6 octahedra, which led to the formation of Nb=O bonds [28]. The peaks at 414 cm^{-1} and 459 cm^{-1} have been attributed to the symmetric stretching $v_s[Nb(O)_2]$ and the asymmetric stretching $v_a[Nb(O)_2]$, respectively. Their occurrence indicated the presence of a small amount of coordinated peroxide on the Nb(V) ions [29]. With increasing calcination temperatures, the peak at 459 cm^{-1} first decreased from 200–400 °C and then disappeared entirely at 500 °C. The peaks at 3753 cm^{-1} and 1559 cm^{-1} have been attributed to the vibration of OH groups v(O–H) of adsorbed water molecules [30], which disappeared after increasing the calcination temperature (as shown in Figure S2).

The FTIR spectrum of GCN shows numerous bands in the 1100–1630 cm^{-1} region corresponding to the typical stretching modes of GCN heterocycles. The FTIR spectra of the heterostructures NBCN-X(X = 1–4) exhibited characteristic peaks of NBO and GCN. However, for NBCN-1 and NBCN-2 the GCN band's peaks were found to be weaker than NBCN-3 and NBCN-4, due to the lower amount of GCN incorporated in the heterostructure. The results were consistent with the XRD results. Moreover, the sharp band at 810 cm^{-1} was associated with the tri-s-triazine forming the GCN structure. The broad band around 3163 cm^{-1} could be associated with the N–H or O–H bonds of the residual amino groups or absorbed H_2O molecules [31,32]. Detailed FTIR spectra are also provided in Table S1.

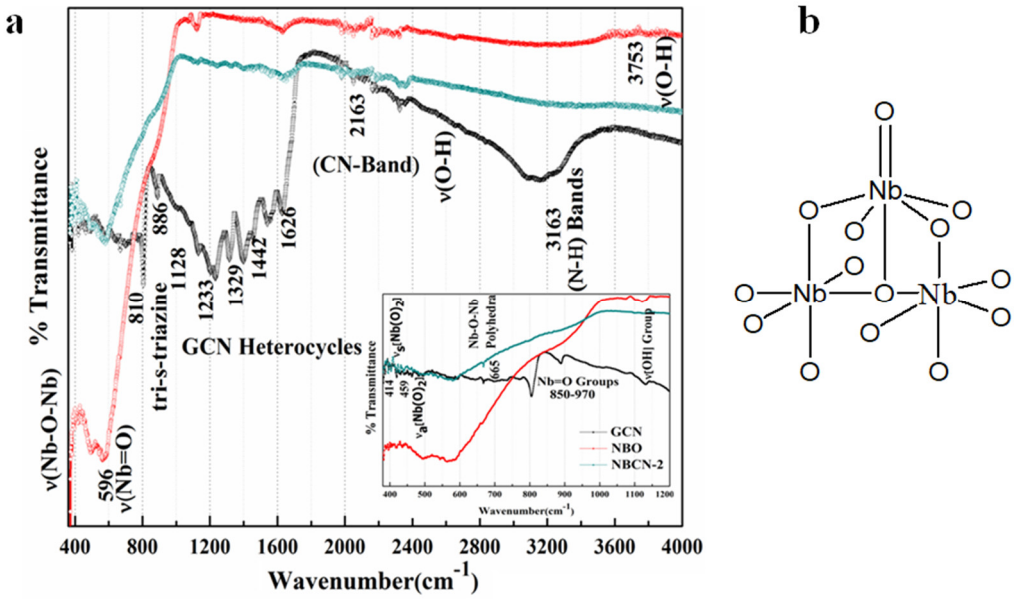

Figure 5. (**a**) FTIR spectra of NBO, GCN and NBCN-2 and (**b**) Highly and slightly distorted NbO_6 octahedra coexist in the structure.

SEM and TEM images of as-synthesized photocatalysts are shown in Figure 6. The bulk of the GCN and the hierarchical nanospheres of NBO can be seen in Figure 6a,b, respectively, while the NBCN heterostructures are given in Figure 6c–f. A significant change in the morphology can be observed for the NBO and NBCN heterostructures. BET analysis helped to further analyze the change in the surface area of bare and heterostructure photocatalysts. The high surface area of NBO-BA gradually decreased with increasing the annealing temperature from 200 to 500 °C (see Table S2). A high annealing temperature favored pore coalescence due to the crystallisation of walls separating mesopores in their structures. The BET surface areas of NBCN-X (X = 1–4) annealed at 200 °C and are provided in Table S3. The specific surface area decreased gradually with the increase in the amount of GCN, due to the low surface area of GCN.

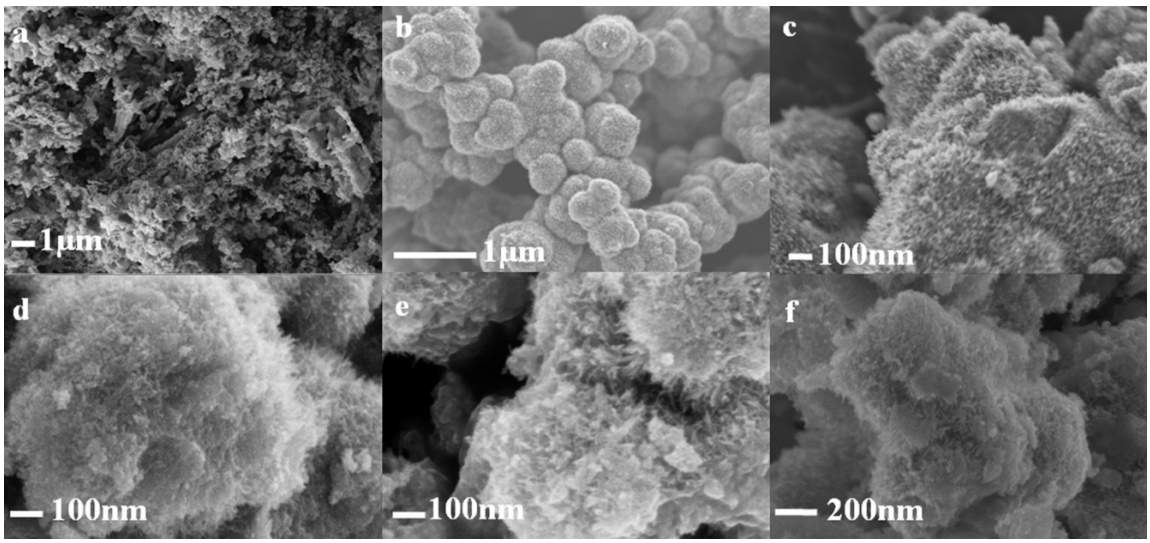

Figure 6. SEM images of (**a**) GCN, (**b**) NBO, (**c**) NBCN-1, (**d**) NBCN-2, (**e**) NBCN-3, and (**f**) NBCN-4.

A TEM analysis for NBO and NBCN-2 was conducted, as shown in Figure 7. For NBO (Figure 7a), the lattice fringes had 0.39 nm d-spacing's corresponding to the (001) lattice plane of Nb_2O_5. A small number of lattice fringes were observed due to the amorphous nature of NBO. The SAED pattern

(Figure 7a inset) indicated that the NBO was in the transforming state from the amorphous to the crystalline phase (consistent with XRD results). More TEM images at different resolutions are provided in Figure S3. For NBCN-2 (Figure 7b), lattice fringes for NBO and GCN were observed. However, due to a smaller amount of GCN, only a few lattice fringes for GCN were observed (0.31 nm d-spacing of (002) plane). The (001) plane of NBO was found to be compatible with the (002) plane of GCN, thus favoring the in-situ growth of NBO on the surface of GCN.

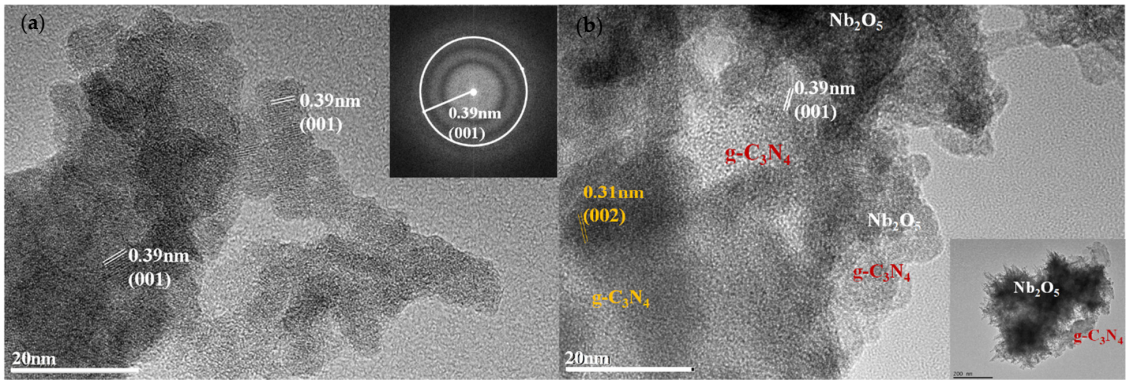

Figure 7. (**a**) HRTEM (high electron transmission electron microscopy) image and SAED (selected area electron diffraction) pattern (inset) of NBO, (**b**) HRTEM image and TEM (inset) image of NBCN-2.

2.3. Photocatalytic Evolution of Molecular H_2

A systematic study was conducted to signify the role of all possible parameters that could change the rate of generated molecular hydrogen (H_2). Initially, the photocatalytic formations of molecular H_2 for P25, GCN, NBO and NBCN-X (X = 1–4) were studied with and without Pt deposition in the presence of TEOA (a hole scavenger). The evolved H_2 is shown in Figure 8a,b, respectively. The total liberated amount in 7 h is also shown in Figure 8c. All heterostructures prepared generated more molecular H_2 than P25, NBO or GCN, both with and without Pt deposition. This increase in the H_2 formation rate with Pt deposition can be taken as evidence for the successful interfacial charge separation. Among all heterostructures, NBCN-2 showed the highest H_2 generation rate of 110 mmol/g·h, which could be associated with both its high surface area and suitable band positions. The evolution rates for other prepared composites: NBCN-1 = 103.27 mmol/g·h, NBCN-3 = 77.88 mmol/g·h, and NBCN-4 = 56.04 mmol/g·h, are also higher than those for P25 = 45.46 mmol/g·h, GCN=33.46 mmol/g·h or NBO= 41.20 mmol/g·h. Thus, the enhanced photocatalytic activity may have been caused by GCN loading acting as a visible light active material and as an efficient electron-hole separator for NBCN prepared heterostructures. However, this effect was only obvious provided that the optimised ratio of GCN and NBO was used.

For P25, the formation rate of molecular H_2 was increased in the first 4 h then a gradual decrease was observed. In comparison to bare materials the H_2 formation rate of P25 was larger than GCN and NBO, i.e., 45.46 mmol/g·h, but the rate was not stable after Pt deposition, as shown in Figure 8a,b, respectively. The H_2 formation rate was also smaller than all heterostructures prepared and the ~66% increase in molecular H_2 evolution rate was observed after Pt deposition, which was less than all heterostructures prepared. Moreover, the prepared composites showed more of a stable increase in the molecular H_2 formation rate than P25. The effect of methanol over platinized P25 could be studied through the Kandiel papers [33,34].

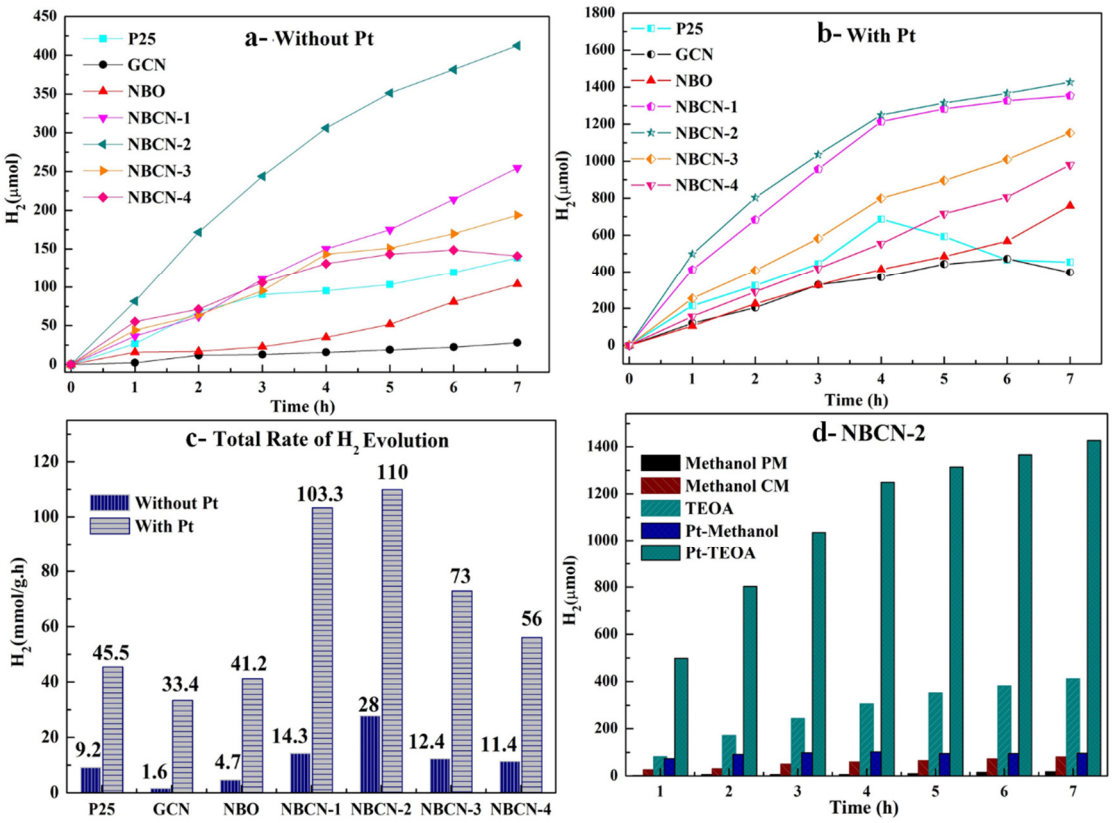

Figure 8. The photocatalytic formation of molecular H_2 of P25, NBO, GCN, NBCN-1, NBCN-2, NBCN-3 and NBCN-4: (**a**) without Pt, (**b**) with Pt deposition, and (**c**) total evolution rate; (**d**) photocatalytic formation of molecular H_2 of NBCN-2, in the presence of methanol and TEOA.

Secondly, to understand the role of the scavenger, the NBCN-2 activity employing methanol as hole scavenger was also investigated with and without Pt deposition. The change in H_2 evolution with time and in comparison with TEOA is shown in Figure 8d. A total of 5.53 mmol/g·h and 9.3 mmol/g·h of H_2 were liberated without and with Pt deposition, respectively. This increase was just 25%, and was 60% with TEOA. Moreover, in the presence of methanol, the H_2 amount was 67% (without Pt) and 85% (with Pt) less than TEOA. In light of the above results, TEOA not only gave higher activity, but also favored interfacial charge separation after Pt deposition. The findings indicated a possible change in the photocatalytic scheme. NBCN-2 results have also been compared with the physically mixed compound (with the same composition) in the presence of methanol. The NBCN-2 photocatalyst and physically mixed photocatalyst with the same ratio of NBO and GCN were used. A drastic change in the evolution rate was observed, as shown in Figure 8d, and more clearly in Figure S4. The NBCN-2 molecular H_2 generation rate showed a 35% increase over the physically mixed photocatalyst. Thus, in-situ heterostructures have higher activity than physically mixed heterostructures, and this can be attributed to good intimate contact. The total generated amount of H_2 for all studied photocatalysts has been provided in Table S4.

The present results have also been compared with previous reports on GCN, NBO and NBCN in the presence of TEOA/Methanol. The comparison is provided in Table 1. A detailed analysis of the table has proven the significance of our work in the following ways: (a) higher molecular H_2 rate in less time, (b) less concentration of photocatalysts and (c) the synthesized heterostructures have a higher molecular H_2 rate than many of them, even without the Pt deposition.

Table 1. A brief comparison of present molecular H_2 evolution rate employing g-C_3N_4 and/or Nb_2O_5.

Photocatalysts	Co-Catalyst	Scavenger	Reaction Conditions [a]	Light Source	H_2 (μmol/h/g)	Ref
Nb_2O_5 **g-C_3N_4** **P25** **Nb_2O_5/g-C_3N_4 (Best Composite)**	Pt (1.0 wt %)	TEOA (10 Vol. %)	45 mL, 10 mg (7 h)	Simulated Solar Lamp	41,200 33,460 45,460 110,000	Present
Cu_2O/g-C_3N_4-Mechanical Composite **Cu_2O (0.05 wt %)-g-C_3N_4-In-Situ Composite** **g-C_3N_4**	Pt (1.0 wt %)	TEOA (10 Vol. %)	180 mL, 100 mg (11 h)	Visible Light	142 241 142	[35]
Pt-g-C_3N_4-TiO_2 **g-C_3N_4-Pt-TiO_2**	Pt (not defined)	TEOA (10 Vol. %)	100 mL, 100 mg	Visible Light (420 nm)	1240 1780	[36]
Urea-polymerized-g-C_3N_4	Pt (3.0 wt %)	TEA (10 Vol. %) nil	100 mL, 80 mg (8 h) 100 mL, 80 mg (25 h)	Simulated Solar Lamp	590 3.13	[37]
Zn-tri-PcNc sensitized g-C_3N_4	Pt (1.0 wt %)	TEOA (10 Vol. %)	10 mL H_2O + 50 mL Ascorbic Acid, 10 mg (10 h)	Infrared 500 nm	12,500	[38]
g-C_3N_4 **NiS/g-C_3N_4**	Pt (2.0 wt %) NiS (1.5 mol %)	TEOA (10 Vol. %)	100 mL, 100 mg	Visible Light (420 nm)	480 450	[39]
g-C_3N_4	Pt (3.0 wt %)	TEOA (10 Vol. %) + K_2HPO_4	270 mL, 50 mg	Visible Light (420 nm)	18,940	[40]
Nb_2O_5/g-C_3N_4 (Best Composite) **Nb_2O_5/g-C_3N_4 (Physically Mixed)**	– Pt (1.0 wt %)	Methanol (10 Vol. %)	45 mL, 10 mg (7 h)	Simulated Solar Lamp	5530 9322 851	Present
Mesoporous Nb_2O_5	Pt (0.5 wt %)	Methanol (12.5 Vol. %)	400 mL, 10 mg (7 h)	Mercury Lamp (200–600 nm)	12,350	[41]
Mesoporous Nb_2O_5 nano particles	Pt (1.0 wt %)	Methanol (9.1 Vol. %)	220 mL, 20 mg (4 h)	Mercury Lamp Internal Irradiation	191	[42]
Mesoporous Nb_2O_5	– Pt (2.0 wt %) CuO NiO	Methanol (1M) + H_2SO_4 (1M)	200 mL, 200 mg (6 h)	White Light Source	1120 510 1405 800	[43]
Mesoporous Nb_2O_5	– Au (1.0 wt %) Pt (1.0 wt %) Cu (1.0 wt %) NiO (1.0 wt %) C	MeOH: H_2O = (1:5)	550 mL, 200 mg (6 h)	UV Light (360 nm) Internal Irradiation	328 2091 4647 1572 709 8.5	[44]

[a] Reaction Conditions: volume of photocatalytic solution, amount of photocatalyst and total time for H_2 evolution.

To estimate the electronic structure and possible interfacial band bending of materials, we conducted Mott–Schottky measurements (C^{-2} versus applied potential). The flat band/conduction band potentials (E_{FB}/E_{CB}), intercepted for NBO and GCN, are −0.61 V (−0.69) and −1.6 (−1.68) V vs. NHE (pH = 7), as shown in Figure 8a. The values have been converted to pH = 7 by using equations Equation (S1) and Equation (S2), respectively. By using the bandgap energy calculated through UV-vis-Absorption, the estimated valence band potentials (E_{VB}) are 2.32 V and 0.88 V for NBO and GCN at pH = 7, respectively (provided in Figure S5). Judging by the bandgap positions, typically a type-II mechanism should be followed, e.g., the photogenerated electrons in GCN could easily move to the NBO conduction band following the reduction there, and the photogenerated holes could easily move from the NBO valence band to the GCN valence band following the oxidation process. However, based on the recent report by Huang, Z.-F et al. [22], when TEOA is adsorbed on the surface the electron transfer is inverted as shown in Figure 1, and hence the Z-Scheme mechanism is followed. Following their results, the NBO electrons recombined with the holes of the GCN and consequently, reduction and oxidation reactions at the GCN and NBO occurred, respectively. The high production rate also favoured the direct Z-Scheme.

We estimated the charge carrier densities (N_D) to understand the interfacial band bending by using the Mott–Schottky slope (Figure 9). For a theoretical overview, the inclination angle of the M–S plot fo GCN was smaller than NBO. Since the relative dielectric constant (ε) was directly proportional to the inclination angle (θ) and inversely proportional to donor density (N_D) of the material. Hence, GCN should have a smaller dielectric constant and a higher donor density than NBO. In the literature, ε ~7–8 for GCN [32] and ε ~38 for pseudohexagonal NBO [45] has been reported. GCN ε is six times larger than NBO, so the N_D for GCN should be around six times larger than NBO. Mathematically, N_D has been calculated by using Equation (1) [46]:

$$N_D = \frac{2}{e_0 \varepsilon_0 \varepsilon} \left[\frac{d(1/C^2)}{dV} \right]^{-1} \quad (1)$$

where, e_0, ε_0, ε and $\frac{d(1/C^2)}{dV}$ are electron charge, vacuum permittivity, material dielectric constant and Mott–Schottky slope, respectively. The approximated values for GCN $N_D \approx 6.1 \times 10^{21}$ cm^{-3} and for NBO $N_D \approx 7.9 \times 10^{20}$ cm^{-3}, have been calculated, i.e., NBO N_D is seven times smaller than GCN, as expected.

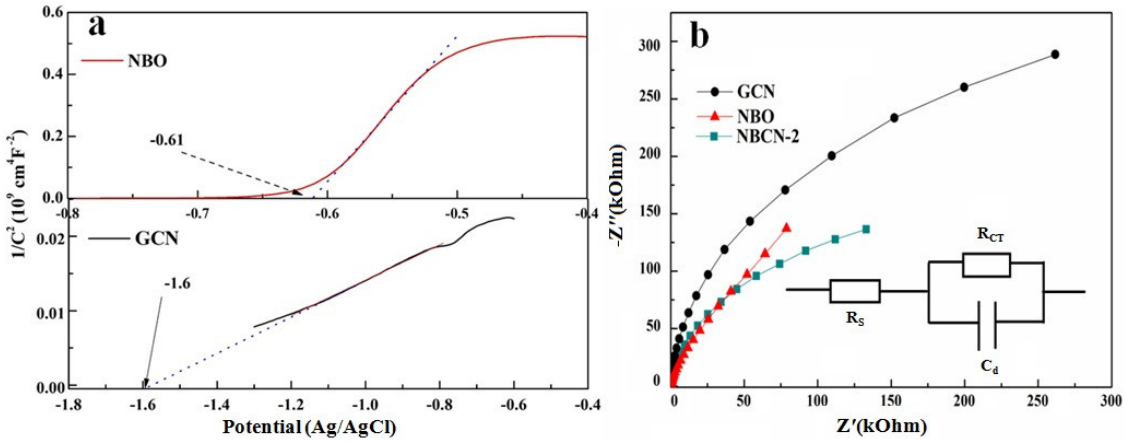

Figure 9. (**a**) Mott–Schottky plot for NBO and GCN at 1000 Hz vs. Ag/AgCl, (**b**) EIS analysis for NBO, GCN and NBCN-2.

For the n-type, due to high donor density, the Fermi level lay close to the bottom of the conduction band. Eventually, upward band bending occurred due to the high electron density of the conduction band and low acceptor density of the valence band. On the other hand, for low donor density of

n-type, the Fermi level lay close to the middle of the bandgap. Moreover, a downward band bending of the conduction band and the valence band occurred. Thus, following the concept, after irradiation, the equilibrium Fermi level (E_F) of NBO and GCN was lying close to the redox potential (−0.41 V) vs. NHE (pH = 7). However, to justify the Z-Scheme and high production rate, fast recombination at the interface and fast charge transfer at the proposed conduction and valence bands should be followed.

Electrochemical Impedance Spectroscopy (EIS) analysis helped to further estimate the recombination and charge transfer process at the working electrode and electrolyte interfaces. Nyquist plots for NBO, GCN and NBCN-2 in the frequency range of 1000 kHz–0.01 Hz under UV-Vis light irradiation have been recorded (Figure 8b). The Randles circuit model [47] has been employed to describe the behavior of the electrode, as shown in the inset of Figure 8b. The arc radius has been associated with charge transfer resistance (R_{CT}) across the interface of working electrode/electrolyte, i.e., the small radius means efficient interfacial charge transfer/slow recombination rate of photogenerated electron/hole pairs. All three electrodes showed explicit arcs and the fitted values of R_{CT} are: NBO = 342 kΩ, GCN = 348 kΩ and NBCN-2 = 159 kΩ. The lowest R_{CT} for NBCN-2 has been recorded, which indicated that the composites have better efficiency of charge transfer than NBO and GCN. The NBO showed slightly better photoactivity than GCN. The large R_{CT} for GCN indicated its poor charge transfer characteristics, which may be associated with a low charge transfer rate leading to the fast recombination of photogenerated electron/hole pairs and poor photoactivity.

Thus, there was two times reduced resistance for the NBCN-2 heterostructures than NBO and GCN, which favored the reduced charge-transfer barrier with an increase in charge carrier density, and hence the Z-scheme system is followed. The proposed energy diagram and mechanism is shown in Figure 10. The proposed mechanism has been associated with the compatible band positions of NBO and GCN, which favored the direct Z-scheme transfer of charges and thus a higher molecular H_2 production rate. That is, the 1 wt % platinizied NBCN heterostructure exhibits a high activity for H_2 generation of 110 mmol/g·h because the direct transfer and recombination of photogenerated electrons in NBO and holes in GCN could greatly extend the lifetime time of carriers. The negative shift of the flat band of NBCN heterojunction (provided in Figure S6) further confirms the proposed Z-scheme mechanism.

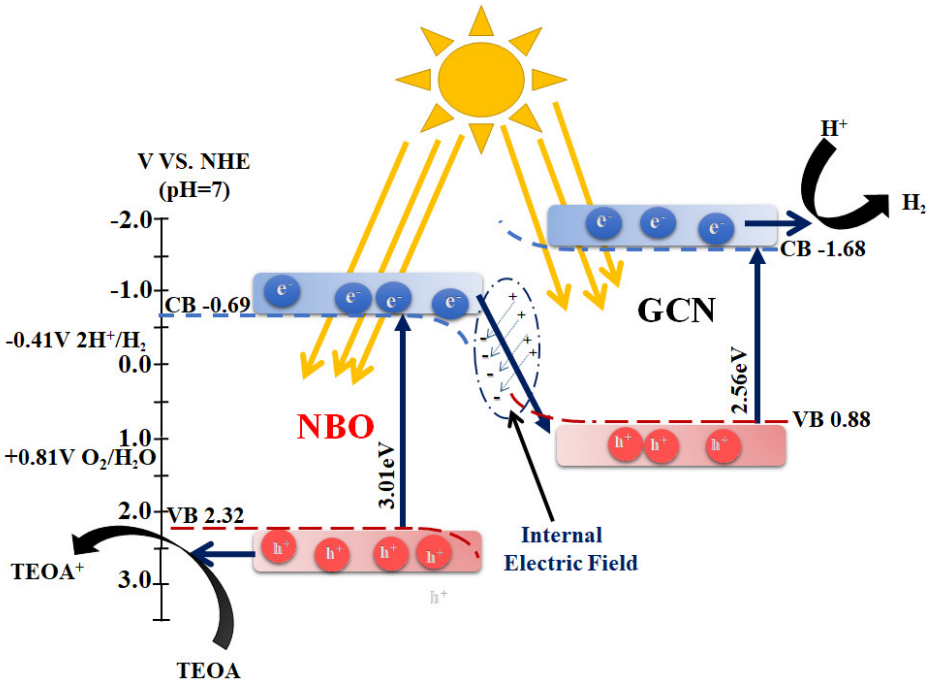

Figure 10. Schematic illustration of possible photocatalytic mechanism.

3. Methods

Niobium pentachloride $NbCl_5$ (99.9%, Sigma Aldrich, Munich, Germany), melamine $C_3H_6N_6$ (99.0%, Sigma Aldrich, Munich, Germany), hydrogen peroxide solution H_2O_2 (30 wt %), nitric acid HNO_3 (60 wt %), Evonil Aeroxide TiO_2 P25, chloroplatinic acid hexahydrate $H_2PtCl_6.6H_2O$ ($\geq$37.05%, Sigma Aldrich, Munich, Germany) and triethanolamine $(HOCH_2CH_2)_3N$ (99.5%, Sigma Aldrich, Munich, Germany) were used without further purification.

3.1. Material Synthesis

3.1.1. Preparation of Nb_2O_5 (NBO)

0.5 g of hygroscopic yellow powder of $NbCl_5$ was added into a mixture of 20 mL de-ionised water and 0.5 mL HNO_3. The solid dissolved immediately yielding a transparent solution. 10 mL of aqueous H_2O_2 solution was added drop-wise into a clear solution under vigorous stirring. The solution became light yellow, confirming the formation of the niobium-peroxo complex (NPC). This solution was diluted to 60 mL by further addition of de-ionised water. The prepared light-yellow solution was subesquently transferred into a 250 mL autoclave and maintained at 110 °C for 24 h in an oven. The synthesised white precipitate was centrifuged and washed several times with de-ionised water. Subsequently, the prepared powder was dried in an oven at 90 °C for 12 h (named as NBO-BA). The resultant NBO-BA samples were further annealed in a muffle furnace at different temperatures ranging from 200 °C to 500 °C for 2 h with a heating rate of 10 °C min^{-1}. In the present work, the photocatalyst annealed at 200 °C has been named as NBO, throughout.

3.1.2. Preparation of g-C_3N_4 (GCN)

10 g of melamine were placed in a crucible with a cover lid on top and then annealed at 550 °C for 3 h in a muffle furnace employing a heating rate of 10 °C min^{-1}. After natural cooling, a yellow powder of bulk g-C_3N_4 was obtained (named as GCN).

3.1.3. Preparation of Nb_2O_5/g-C_3N_4 (NBCN)

The Nb_2O_5/g-C_3N_4 heterostructures named as NBCN-X (where X = 1, 2, 3, 4) were prepared by using different amounts of GCN. Typically, 2.5 mg of NBO-BA were obtained by hydrothermal synthesis. Therefore, for the heterostructure preparations, the selected amount of GCN was added to the prepared solution of NBO-BA, i.e., X: 1 = 5 wt %, 2 = 10 wt %, 3 = 30 wt % and 4 = 60 wt %. The synthesis process was as follows: initially, GCN suspension was prepared in 20 mL of de-ionised water following the ultra-sonication for 30 min. Then, the prepared GCN suspension was added to a light-yellow solution of NPC under continuous stirring. The amount was adjusted to 60 mL by further addition of de-ionised water and stirring for 30 min. Choosing pH = 0.7 should assure the positive and negative surface charges have been developed over GCN and NPC, respectively, for favorable interface development. The prepared concentrated solution was subsequently transferred to a 250 mL autoclave and maintained at the 110 °C for 24 h in the oven. After washing and drying at 90 °C for 12 h, a light-yellow powder is obtained, which was further annealed at 200 °C for 2 h in a muffle furnace with a 10 °C min^{-1} ramp rate.

3.2. Photodeposition of Platinum (Pt)

The photo-deposition technique was applied to deposit 1 wt % platinum (Pt) on the samples. Hexachloroplatinic acid ($H_2PtCl_6 \cdot 6H_2O$) was used as the Pt precursor and methanol as a reducing agent. The calculated amounts of $H_2PtCl_6 \cdot 6H_2O$ and the photocatalyst were added to 10 vol/vol. % of aqueous methanol solution. The resulting suspension was transferred into a closed reactor and placed under UV-light for 12 h with continuous stirring. The suspension was washed several times

with de-ionised water to remove non-deposited Pt and subsequently with ethanol. The obtained Pt loaded photocatalysts were dried in an oven for 12 h at 90 °C.

3.3. Material Characterization

A Bruker (D8 Advance) instrument using Cu Kα (α = 0.15406 nm) radiation was used to record the X-ray diffraction (XRD) data of the as-synthesized samples. Scanning electron microscopy (SEM, JEOL JSM-6700F, JEOL, Tokyo, Japan) with a LEI detector (Lower Secondary Electron Image) was employed to analyze the morphologies. Transmission electron microscopy (TEM), using an FEI Tecnai G2 F20 microscope operating at 200 kV was used to characterise the samples further. Micrographs were taken in bright field (BF) and in a selected area electron diffraction mode. A Varian Cary 100 Bio was used to measure the UV–vis absorption spectra. A Bruker Vertex 80v spectrophotometer (Bruker, Billerica, MA, USA) was used to measure the FTIR spectra from 4000 to 400 cm^{-1} in vacuum.

3.4. Photocatalytic Molecular Hydrogen (H_2) Formation

The prepared photocatalysts without and with Pt deposits were used to conduct photocatalytic molecular hydrogen (H_2) evolution reactions. In a typical experimental run, 0.01 g of the photocatalyst were added into 45 mL of de-ionised water (maintaining pH 5.6). Methanol or TEOA were added resulting in a suspension which contains 10 vol % of a hole scavenger. The suspension inside the photoreactor was thoroughly degassed for 30 min with Ar to remove air and then stirred for 30 min in the dark to establish the adsorption equilibrium. Afterwards, the photoreactor was placed under a Xenon light source (1000 W, 1.5G) suitable to simulate solar light for 7 h. The temperature was maintained constant by using a homemade cooling system. The evolved amounts of H_2 were measured every 1 h by using a gas chromatograph (Shimadzu 8A (Shimadzu, Kyoto, Japan) equipped with a TCD detector and a 5 Å molecular sieve packed column; Ar was used as the carrier gas).

3.5. Photoelectrochemical Measurements

The photoelectrochemical (PEC) measurements were conducted by using an electrochemical workstation (CHI-660B, CH Instruments, Inc., Austin, TX, USA) accompanying a ZAHNER PECC-2 reactor and 450W xenon lamp as a light source. Moreover, a standard three-compartment cell (consisting of a photo-/working electrode (WE), a Pt wire counter electrode (CE) and an Ag/AgCl reference electrode (RE)) with 0.2 M Na_2SO_4 electrolyte solution (pH = 5.6) were used. The working electrode was prepared using a screen-printing method and then annealed at 400 °C for 2 h to remove organic chemicals. Mott–Schottky measurements were performed at a frequency range of 10–1000 Hz with 10 mV amplitude. Electrochemical impedance spectra were obtained under irradiation at open circuit voltage over a frequency range from 1000 Hz to 0.01 Hz, with an AC voltage at 250 mV vs. Ag/AgCl reference electrode.

4. Conclusions

Z-scheme Nb_2O_5/g-C_3N_4 heterostructures with excellent molecular H_2 production activity were prepared via in-situ hydrothermal syntheses. The prepared heterostructures exhibited excellent photocatalytic activity compared to individual g-C_3N_4 and Nb_2O_5 under simulated solar light illumination. The highest reported H_2 evolution rate was 110 mmol/g·h (7.7 mmol). We found that by increasing the amount of g-C_3N_4, the molecular H_2 production rate decreased, indicating more intimidating interface development does not favor photocatalytic reactions. However, the molecular H_2 evolution rate for all prepared heterostructures was higher than many other semiconductors reported in the literature. Moreover, we justified our results by a reduced recombination rate, high charge carrier density and complemented band positions. For future work, we suggest that the various heterojunction materials possessing diverse structural morphology exhibiting a higher photocatalytic activity be prepared by the simple methodology described here. These studies will pave the way

for a new dimension in photocatalytic studies of Nb_2O_5 and g-C_3N_4 nanocomposites for enhanced molecular H_2 production.

Supplementary Materials: The following are available online at http://www.mdpi.com/2073-4344/9/2/169/s1, Figure S1: XRD patterns BA and AA at different calcination temperatures, Figure S2: FTIR spectra of all photocatalysts, Figure S3: TEM images of NBO, Figure S4: Molecular H_2 generation of NBCN-2, Chemical and Physical Mixing in the presence of methanol, Figure S5: Bandgap vs. photon energy by UV-vis-Diffuse Absorption Spectra of a) NBO, GCN, NBCN-1, NBCN-2, NBCN-3, and NBCN-4 and b) with the change in the annealing temperature, Figure S6: Mott-Schottky plot of NBO and NBCN-2, Table S1: Associated Bands in FTIR Spectra, Table S2: Specific surface area (m^2/g) of samples with different calcination temperatures, Table S3: Specific surface area of NBO and NBCN-X (X = 1–4) without calcination, Table S4: Liberated Amount of H_2 after 7h with and without Pt, Equation (S1) and Equation (S2).

Author Contributions: F.I. conceived, designed and performed the experiments; F.K.B. and M.T. analyzed the data; R.D. contributed reagents/materials/analysis tools; F.I., R.D. and D.B. wrote the paper. Substantial paper changes have been made by Ralf and Bahnemann.

Funding: The work was supported by the Alexendar Von Humboldt Foundation (Project No. 60421802) and PSF/NSFC/Eng-P-UoL(02).

Conflicts of Interest: We declare no conflict of interest.

References

1. Fujishima, A.; Honda, K. Electrochemical Photolysis of Water at a Semiconductor Electrode. *Nature* **1972**, *238*, 37. [CrossRef] [PubMed]
2. Yu, J.; Qi, L.; Jaronie, M. Hydrogen Production by Photocatalytic Water Splitting over Pt/TiO_2 Nanosheets with Exposed (001) Facets. *J. Phys. Chem. C* **2010**, *114*, 13118–13125. [CrossRef]
3. Cho, I.S.; Chen, Z.; Forman, A.J.; Kim, D.R.; Rao, P.M.; Jaramillo, T.F.; Zheng, X. Branched TiO_2 Nanorods for Photoelectrochemical Hydrogen Production. *Nano Lett.* **2011**, *11*, 4978–4984. [CrossRef] [PubMed]
4. Luo, J.; Steier, L.; Son, M.K.; Schreier, M.; Mayer, M.T.; Michael, G. Cu_2O Nanowire Photocathodes for Efficient and Durable Solar Water Splitting. *Nano Lett.* **2016**, *16*, 1848–1857. [CrossRef] [PubMed]
5. Ye, R.; Fang, H.; Zheng, Y.-Z.; Li, N.; Wang, Y.; Tao, X. Fabrication of $CoTiO_3$/g-C_3N_4 Hybrid Photocatalysts with Enhanced H_2 Evolution: Z-Scheme Photocatalytic Mechanism Insight. *ACS Appl. Mater. Interfaces* **2016**, *8*, 13879–13889. [CrossRef] [PubMed]
6. Tahir, M.; Cao, C.; Butt, F.K.; Butt, S.; Idrees, F.; Ali, Z.; Aslam, I.; Tanveer, M.; Mahmood, A.; Mahmood, N. Large scale production of novel g-C_3N_4 micro strings with high surface area and versatile photodegradation ability. *CrystEngComm* **2014**, *16*, 1825–1830. [CrossRef]
7. Tahir, M.; Cao, C.; Butt, F.K.; Idrees, F.; Mahmood, N.; Ali, Z.; Aslam, I.; Tanveer, M.; Rizwan, M.; Mahmood, T. Tubular graphitic-C_3N_4: A prospective material for energy storage and green photocatalysis. *J. Mater. Chem. A* **2013**, *1*, 13949–13955. [CrossRef]
8. Yan, J.; Wu, G.; Guan, N.; Li, L. Nb_2O_5/TiO_2 heterojunctions: synthesis strategy and photocatalytic activity. *Appl. Catal. B* **2014**, *152*, 280–288. [CrossRef]
9. Tahir, M.; Cao, C.; Mahmood, N.; Butt, F.K.; Mahmood, A.; Idrees, F.; Hussain, S.; Tanveer, M.; Ali, Z.; Aslam, I. Multifunctional g-C_3N_4 nanofibers: A template-free fabrication and enhanced optical, electrochemical, and photocatalyst properties. *ACS Appl. Mater. Interfaces* **2013**, *6*, 1258–1265. [CrossRef]
10. Sridharan, K.; Jang, E.; Park, T.J. Novel visible light active graphitic C_3N_4–TiO_2 composite photocatalyst: Synergistic synthesis, growth and photocatalytic treatment of hazardous pollutants. *Appl. Catal. B* **2013**, *142–143*, 718–728. [CrossRef]
11. Hou, Y.; Zhu, Y.; Xu, Y.; Wang, X. Photocatalytic hydrogen production over carbon nitride loaded with WS_2 as cocatalyst under visible light. *Appl. Catal. B* **2014**, *156–157*, 122–127. [CrossRef]
12. Bai, Y.; Wang, P.-Q.; Liu, J.-Y.; Liu, X.-J. Enhanced photocatalytic performance of direct Z-scheme BiOCl-g-C_3N_4 photocatalysts. *RSC Adv.* **2014**, *4*, 19456–19461. [CrossRef]
13. Aslam, I.; Cao, C.; Tanveer, M.; Khan, W.S.; Tahir, M.; Abid, M.; Idrees, F.; Butt, F.K.; Ali, Z.; Mahmood, N. The synergistic effect between WO_3 and g-C_3N_4 towards efficient visible-light-driven photocatalytic performance. *New J. Chem.* **2014**, *38*, 5462–5469. [CrossRef]
14. Katsumata, H.; Tachi, Y.; Suzuki, T.; Kaneco, S. Z-scheme photocatalytic hydrogen production over WO_3/g-C_3N_4 composite photocatalysts. *RSC Adv.* **2014**, *4*, 21405–21409. [CrossRef]

15. Acar, C.; Dincer, I.; Naterer, G.F. Review of photocatalytic water-splitting methods for sustainable hydrogen production. *Int. J. Energy Res.* **2016**, *40*, 1449–1473. [CrossRef]
16. Idrees, F.; Cao, C.; Ahmed, R.; Butt, F.K.; Butt, S.; Tahir, M.; Tanveer, M.; Aslam, I.; Ali, Z. Novel nano-flowers of Nb_2O_5 by template free synthesis and enhanced photocatalytic response under visible light. *Sci. Adv. Mater.* **2015**, *7*, 1298–1303. [CrossRef]
17. Idrees, F.; Hou, J.; Cao, C.; Butt, F.K.; Shakir, I.; Tahir, M.; Idrees, F. Template-free synthesis of highly ordered 3D-hollow hierarchical Nb_2O_5 superstructures as an asymmetric supercapacitor by using inorganic electrolyte. *Electrochim. Acta* **2016**, *216*, 332–338. [CrossRef]
18. Lam, S.-M.; Sin, J.-C.; Satoshi, I.; Abdullah, A.Z.; Mohamed, A.R. Enhanced sunlight photocatalytic performance over Nb_2O_5/ZnO nanorod composites and the mechanism study. *Appl. Catal. A* **2014**, *471*, 126–135. [CrossRef]
19. Hong, Y.; Li, C.; Zhang, G.; Meng, Y.; Yin, B.; Zhao, Y.; Shi, W. Efficient and stable Nb_2O_5 modified g-C_3N_4 photocatalyst for removal of antibiotic pollutant. *Chem. Eng. J.* **2016**, *299*, 74–84. [CrossRef]
20. Huang, Q.-Z.; Wang, J.-C.; Wang, P.-P.; Yao, H.-C.; Li, Z.-J. In-situ growth of mesoporous Nb_2O_5 microspheres on g-C_3N_4 nanosheets for enhanced photocatalytic H_2 evolution under visible light irradiation. *Int. J. Hydrogen Energy* **2017**, *42*, 6683–6694. [CrossRef]
21. Low, J.; Jiang, C.; Cheng, B.; Wageh, S.; Al-Ghamdi, A.A.; Yu, J. A Review of Direct Z-Scheme Photocatalysts. *Small Methods* **2017**, *1*, 1700080. [CrossRef]
22. Huang, Z.-F.; Song, J.; Wang, X.; Pan, L.; Li, K.; Zhang, X.; Wang, L.; Zou, J.-J. Switching charge transfer of C_3N_4/$W_{18}O_{49}$ from type-II to Z-scheme by interfacial band bending for highly efficient photocatalytic hydrogen evolution. *Nano Energy* **2017**, *40*, 308–316. [CrossRef]
23. Huang, Y.-T.; Cheng, R.; Zhai, P.; Lee, H.; Chang, Y.-H.; Feng, S.-P. Solution-Based Synthesis of Ultrasmall Nb_2O_5 Nanoparticles for Functional Thin Films in Dye-Sensitized and Perovskite Solar Cells. *Electrochim. Acta* **2017**, *236*, 131–139. [CrossRef]
24. Passoni, L.C.; Siddiqui, M.R.H.; Steiner, A.; Kozhevnikov, I.V. Niobium peroxo compounds as catalysts for liquid-phase oxidation with hydrogen peroxide. *J. Mol. Catal. A: Chem.* **2000**, *153*, 103–108. [CrossRef]
25. Narendar, Y.; Messing, G.L. Synthesis, decomposition and crystallization characteristics of peroxo− citrato− niobium: an aqueous niobium precursor. *Chem. Mater.* **1997**, *9*, 580–587. [CrossRef]
26. Silva, G.; Carvalho, K.; Lopes, O.; Ribeiro, C. g-C3N4/Nb2O5 heterostructures tailored by sonochemical synthesis: Enhanced photocatalytic performance in oxidation of emerging pollutants driven by visible radiation. *Appl. Catal. B Environ.* **2017**, *216*, 70–79.
27. Lopes, O.; Paris, E.; Ribeiro, C. Synthesis of Nb_2O_5 Nanoparticles Through the Oxidant Peroxide Method Applied to Organic Pollutant Photodegradation: A Mechanistic Study. *Appl. Catal. B* **2014**, *144*, 800–808. [CrossRef]
28. Jehng, J.M.; Wachs, I.E. Niobium oxide solution chemistry. *J. Raman Spectrosc.* **1991**, *22*, 83–89. [CrossRef]
29. Compton, O.C.; Osterloh, F.E. Niobate nanosheets as catalysts for photochemical water splitting into hydrogen and hydrogen peroxide. *J. Phys. Chem. C* **2008**, *113*, 479–485. [CrossRef]
30. Nakajima, K.; Fukui, T.; Kato, H.; Kitano, M.; Kondo, J.N.; Hayashi, S.; Hara, M. Structure and Acid Catalysis of Mesoporous Nb_2O_5·nH_2O. *Chem. Mater.* **2010**, *22*, 3332–3339. [CrossRef]
31. Cui, Y.; Ding, Z.; Liu, P.; Antonietti, M.; Fu, X.; Wang, X. Metal-free activation of H_2O_2 by g-C_3N_4 under visible light irradiation for the degradation of organic pollutants. *Phys. Chem. Chem. Phys.* **2012**, *14*, 1455–1462. [CrossRef] [PubMed]
32. Giannakopoulou, T.; Papailias, I.; Todorova, N.; Boukos, N.; Liu, Y.; Yu, J.; Trapalis, C. Tailoring the energy band gap and edges' potentials of g-C_3N_4/TiO_2 composite photocatalysts for NO_x removal. *Chem. Eng. J.* **2017**, *310*, 571–580. [CrossRef]
33. Kandiel, T.A.; Dillert, R.; Robben, L.; Bahnemann, D.W. Photonic efficiency and mechanism of photocatalytic molecular hydrogen production over platinized titanium dioxide from aqueous methanol solutions. *Catal. Today* **2011**, *161*, 196–201. [CrossRef]
34. Kandiel, T.A.; Ivanova, I.; Bahnemann, D.W. Long-term investigation of the photocatalytic hydrogen production on platinized TiO_2: An isotopic study. *Energy Environ. Sci.* **2014**, *7*, 1420–1425. [CrossRef]
35. Chen, J.; Shen, S.; Guo, P.; Wang, M.; Wu, P.; Wang, X.; Guo, L. In-situ reduction synthesis of nano-sized Cu_2O particles modifying g-C_3N_4 for enhanced photocatalytic hydrogen production. *Appl. Catal. B* **2014**, *152–153*, 335–341. [CrossRef]

36. Chai, B.; Peng, T.; Mao, J.; Li, K.; Zan, L. Graphitic carbon nitride (g-C_3N_4)-Pt-TiO_2 nanocomposite as an efficient photocatalyst for hydrogen production under visible light irradiation. *Phys. Chem. Chem. Phys.* **2012**, *14*, 16745–16752. [CrossRef] [PubMed]
37. Zhang, Y.; Liu, J.; Wu, G.; Chen, W. Porous graphitic carbon nitride synthesized via direct polymerization of urea for efficient sunlight-driven photocatalytic hydrogen production. *Nanoscale* **2012**, *4*, 5300–5303. [CrossRef]
38. Zhang, X.; Yu, L.; Zhuang, C.; Peng, T.; Li, R.; Li, X. Highly Asymmetric Phthalocyanine as a Sensitizer of Graphitic Carbon Nitride for Extremely Efficient Photocatalytic H_2 Production under Near-Infrared Light. *ACS Catal.* **2014**, *4*, 162–170. [CrossRef]
39. Chen, Z.; Sun, P.; Fan, B.; Zhang, Z.; Fang, X. In Situ Template-Free Ion-Exchange Process to Prepare Visible-Light-Active g-C_3N_4/NiS Hybrid Photocatalysts with Enhanced Hydrogen Evolution Activity. *J. Phys. Chem. C* **2014**, *118*, 7801–7807. [CrossRef]
40. Liu, G.; Wang, T.; Zhang, H.; Meng, X.; Hao, D.; Chang, K.; Li, P.; Kako, T.; Ye, J. Nature-Inspired Environmental "Phosphorylation" Boosts Photocatalytic H_2 Production over Carbon Nitride Nanosheets under Visible-Light Irradiation. *Angew. Chem. Int. Ed.* **2015**, *54*, 13561–13565. [CrossRef]
41. Chen, X.; Yu, T.; Fan, X.; Zhang, H.; Li, Z.; Ye, J.; Zou, Z. Enhanced activity of mesoporous Nb_2O_5 for photocatalytic hydrogen production. *Appl. Surf. Sci.* **2007**, *253*, 8500–8506. [CrossRef]
42. Sreethawong, T.; Ngamsinlapasathian, S.; Lim, S.H.; Yoshikawa, S. Investigation of thermal treatment effect on physicochemical and photocatalytic H_2 production properties of mesoporous-assembled Nb_2O_5 nanoparticles synthesized via a surfactant-modified sol–gel method. *Chem. Eng. J.* **2013**, *215–216*, 322–330. [CrossRef]
43. Pai, Y.-H.; Fang, S.-Y. Preparation and characterization of porous Nb_2O_5 photocatalysts with CuO, NiO and Pt cocatalyst for hydrogen production by light-induced water splitting. *J. Power Sources* **2013**, *230*, 321–326. [CrossRef]
44. Lin, H.-Y.; Yang, H.-C.; Wang, W.-L. Synthesis of mesoporous Nb_2O_5 photocatalysts with Pt, Au, Cu and NiO cocatalyst for water splitting. *Catal. Today* **2011**, *174*, 106–113. [CrossRef]
45. Manuspiya, H. Electrical Properties of Niobium Based Oxides-Ceramics and Single Crystal Fibers Grown by the Laser-Heated Pedestal Growth (LHPG) Technique. Ph.D. Thesis, Penn State University, University Park, PA, USA, 4 April 2003.
46. Gelderman, K.; Lee, L.; Donne, S.W. Flat-Band Potential of a Semiconductor: Using the Mott–Schottky Equation. *J. Chem. Educ.* **2007**, *84*, 685. [CrossRef]
47. Mousa, G.; Golnaraghi, F.; DeVaal, J.; Young, A. Detecting proton exchange membrane fuel cell hydrogen leak using electrochemical impedance spectroscopy method. *J. Power Sources* **2014**, *246*, 110–116. [CrossRef]